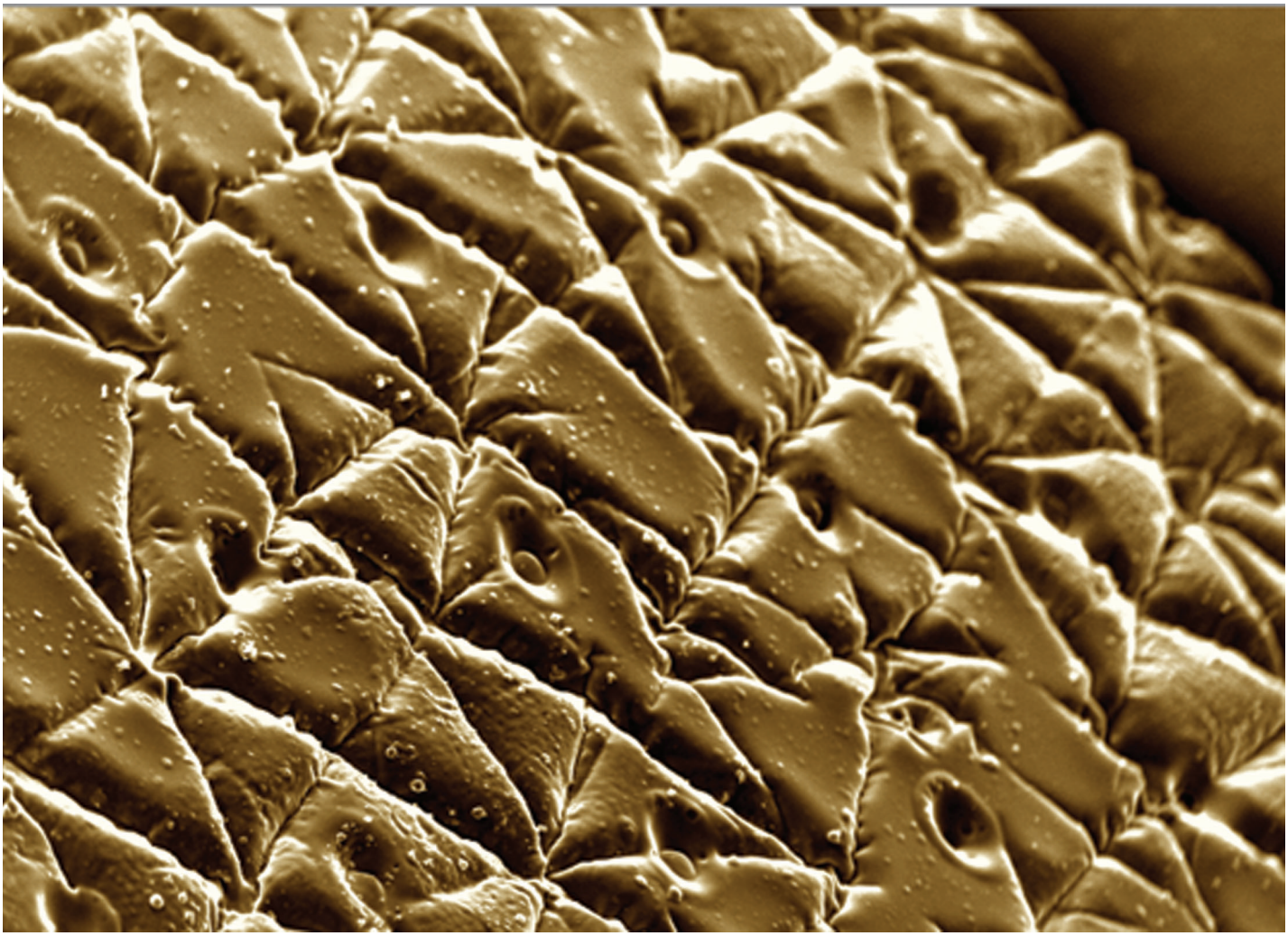

Featuring work from the groups of Prof. Jason Heikenfeld and Prof. Ian Papautsky of the Ohio Center for Microfluidic Innovation at the University of Cincinnati, and Dr. Rajesh Naik and Dr. Joshua Hagen of the U.S. Air Force Research Laboratory.

Title: Artificial Microfluidic Skin for In Vitro Perspiration Simulation and Testing

To expedite development of any skin wearable material, product, or device, an artificial perspiration (sweat) simulator can provide improved ease, cost, control, flexibility, and reproducibility in comparison to human or animal tests. An artificial skin is presented for in-vitro perspiration tests, capable of skin-like texture, wetting, sweat pore-density, and sweat rates.

As featured in:

See Jason Heikenfeld *et al.*, *Lab Chip,* 2013, **13**, 1868.

RSC Publishing

www.rsc.org/loc

Registered Charity Number 207890

Lab on a Chip

RSC Publishing

PAPER

Artificial microfluidic skin for *in vitro* perspiration simulation and testing

Cite this: *Lab Chip*, 2013, **13**, 1868

Linlin Hou,[a] Joshua Hagen,[b] Xiao Wang,[a] Ian Papautsky,[a] Rajesh Naik,[c] Nancy Kelley-Loughnane[b] and Jason Heikenfeld*[a]

Received 6th November 2012,
Accepted 18th March 2013

DOI: 10.1039/c3lc41231h

www.rsc.org/loc

To expedite development of any skin wearable material, product, or device, an artificial perspiration (sweat) simulator can provide improved ease, cost, control, flexibility, and reproducibility in comparison to human or animal tests. Reported here is a human perspiration mimicking device including microreplicated skin-texture. A bottom 0.2 μm track etched polycarbonate membrane layer provides flow-rate control while a top photo-curable layer provides skin-like features such as sweat pore density, hydrophobicity, and wetting hysteresis. Key capabilities of this sweat simulator include: constant 'sweat' rate density without bubble-point variation even down to ~1 L h^{-1} m^{-2}; replication of the 2 pores mm^{-2} pore-density and the ~50 μm texture of human skin; simple gravity-fed flow control; low-cost and disposable construction.

Introduction

Skin is the largest organ in humans and in addition to providing protection, sensation, and insulation; it is also able to regulate body temperature through perspiration (sweat). Sweat is dominated by eccrine glands which number several million over most of the body surface, each gland having dimensions that are microfluidic in nature (several mm long, and 10's of μm in diameter).[1] Interest continues to grow in the physiology of sweat, for a very diverse set of applications: (1) bioactivity and clogging related to cosmetics and other topical products/medicines;[2–4] (2) textile, clothing, and personal care product design,[5] particularly those requiring a high sweat venting rate;[6] (3) drug testing;[7–10] (4) a newly found and rich source of disease and health biomarkers;[11,12] (5) wearable health sensors.[13–16] However, human subject testing for the development of these applications is time and cost intensive. Furthermore, in such testing there is huge variance in the sweat rate density and chemical/molecular composition.[17] There are many forms of *in vitro*[18] or artificial substitutes for testing with other types of body fluids, but remarkably there is a lack of a device which can accurately mimic human sweating. We speculate that this lack of a sweat simulation device can be traced to three technical challenges: (1) sweat rate densities are incredibly slow (*e.g.* 0.75 L h^{-1} m^{-2} for runners[17]) compared to the flow rate densities typically generated by commercial porous membranes (*e.g.* 100s to 1000s of L h^{-1} m^{-2} for track etched membranes[19,20]); (2) commercially available membranes do not provide the surface energy, pore density, nor texture representative of wetting on human skin; (3) membranes suffer from bubble-point thresh-holding of flow which at low flow rates causes a very small percentage of pores to dominate the entire flow of fluid.

We have created the first artificial microfluidic skin for *in vitro* sweat simulation and testing (Fig. 1). In addition to utility for cosmetic, textile, medical, and other applications, our motivation also stems from the need for rapid and repeatable test protocols for our own burgeoning work in wearable sweat biomarker sensors.[21–23] Furthermore, several of the sweat simulators described herein have been provided to an industry partner and successfully used for *in vitro* testing of a new hydration monitoring device. The sweat simulator employs a simple bi-layer membrane design to resolve all drawbacks associated with use of commercial membranes. As shown in Fig. 1b, a first layer creates a pressure drop and therefore a constant sweat flow (comparable to the secretory portion of a sweat gland shown in Fig. 1a), and second top layer provides the requisite pore density and skin-replicated wetting surface. Characterization of the sweat simulator also shows agreement with a simple theoretical model, and therefore the sweat simulator can be rapidly and predictably redesigned/adapted for multiple body surface areas, sweat rate densities, and solute compositions.

Device design and theoretical model

As stated in the introduction, our key design requirements include replication of skin texture, sweat pore density, skin-like surface wettability, and the most challenging requirement

[a]*School of Electronic and Computing Systems, University of Cincinnati, OH 45221, USA. E-mail: heikenjc@ucmail.uc.edu*
[b]*Air Force Research Laboratory, 711th Human Performance Wing, Wright Patterson AFB, OH 45433, USA*
[c]*Air Force Research Laboratory, Materials and Manufacturing Directorate, Wright Patterson AFB, OH 45433, USA*

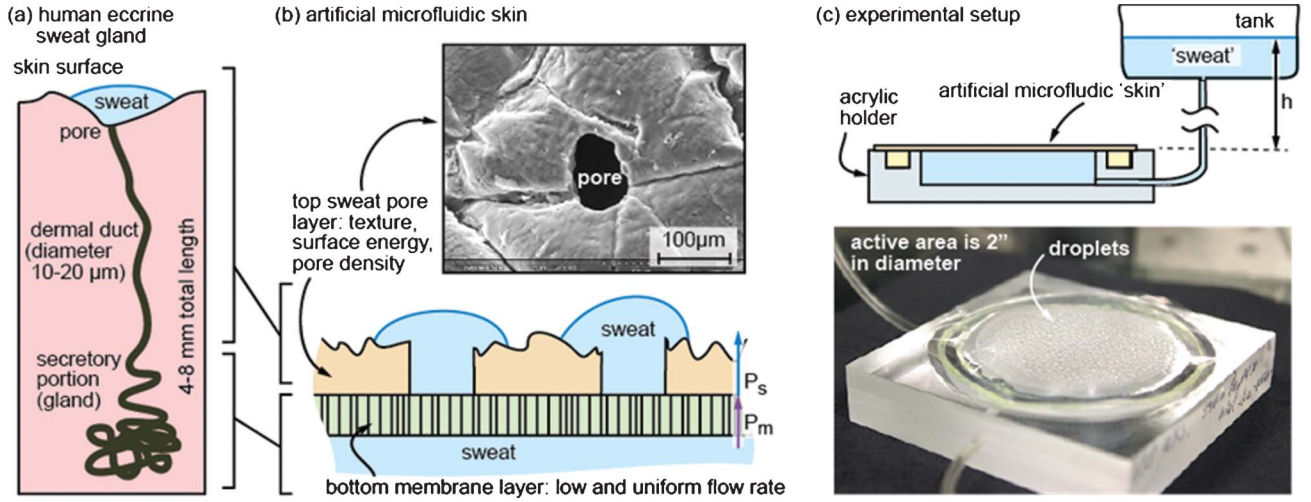

Fig. 1 (a) Diagram of human eccrine sweat gland, (b) diagram and SEM photo of fabricated bi-layer artificial microfluidic 'skin' membrane; and (c) diagram of 'sweat' simulation experimental setup and photo of an operating sweat simulator.

of uniform flow rate among all pores even at the very low flow rates associated with human sweating. The incorrect choice of a single-layer design (Fig. 2a) is first discussed. Any set of pores with different diameters ($D_{S1} > D_{S2}$) will exhibit different Laplace pressures ($P_{L1} = 4\gamma\cos(\theta)/D_1 < P_{L2} = 4\gamma\cos(\theta)/D_2$). As a result, the larger diameter pore will have less Laplace pressure and will first activate with fluid flow (Q_1). Under low flow rate conditions flow resistance is small and the larger diameter pore will continue to provide 100% of the fluid flow as flow from the smaller diameter pore is prevented ($Q_2 \sim 0$) by its higher Laplace pressure. Conversely, under high flow rate conditions, different Laplace pressures will be less consequential as the high pressure associated with high-flow rate will dominate over Laplace pressure, and activate all pores simultaneously regardless of diameter. This higher-pressure/flow-rate test is similar to the 'bubble point' test for a membrane, but is irrelevant to the very low flow rate densities associated with sweating (<1 L h^{-1} m^{-2}). Both the low and high flow rate conditions described were experimentally seen with a single-layer design. We evaluated numerous commercial membranes and found none which came even close to providing both: (1) pore density similar to sweat pores in skin; (2) uniform flow from all pores at the low flow rates associated with sweating. For most commercial membranes, flow would dominate at only very few locations (<1%) creating large/tall droplets that would then activate additional pores only as the few and large growing droplets wetted over them. One might propose to use a membrane with super-wetting (Young's angle of 0°) to eliminate Laplace pressure effects and non-uniform flow from pores, but this is then no-longer representative of wetting on the surface of skin. A novel approach is needed.

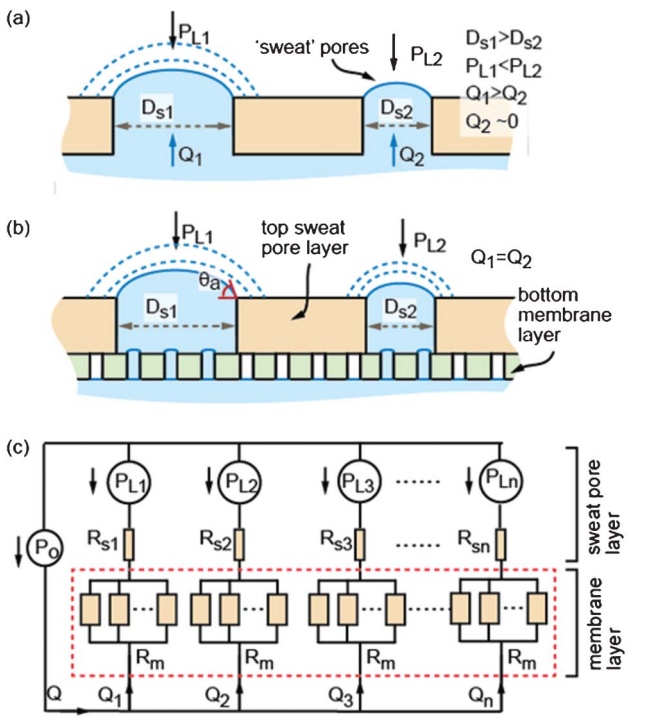

Fig. 2 Illustration of flow through 'sweat pores' in (a) a single layer of 'sweat' pores and (b) a bi-layer approach. Provided in (c) is a resistance network model of the bi-layer approach shown in (b).

Our approach to overcome the Laplace pressure variance among the 'sweat' pores is a bi-layer membrane design as shown in Fig. 2b. The bottom membrane mimics the flow-rate of the secretory portion of a sweat gland while the top membrane provides the proper pore-density and surface energy/texture. The bottom membrane dominates the fluid pressure drop and therefore creates a constant flow through the top membrane. In addition, the following finer design considerations must be implemented. First, the bottom membrane pores should be small enough such that their flow-induced pressure drop is >10× larger than any pressure drop induced by the large pores of the top layer (therefore

promoting uniform flow rate at all pores). Secondly, the small pores in the bottom membrane should be of density adequate such that each large pore in the top layer should statistically average a similar number of small pores beneath it. Thirdly, the bottom membrane must be adequately hydrophilic that the fluid flow can be activated at low pressure and spread on top of the bottom membrane immediately to merge and activate all large pores in the top layer. Commercially available hydrophilic track etched polycarbonate membranes meet these requirements for the bottom membrane, and are available with pore dimensions ranging from 0.01 to 30 μm. As will be discussed in the fabrication section, the top layer will be formed by laser milling and microreplication, and bonded to the bottom membrane.

Next, a pumping mechanism was needed. A simple gravity fed approach was chosen (similar to an intravenous drip-bag) to provide a constant fluid pressure at a very low flow rate for continuous perspiration simulation, which syringe pumps generally fail to provide. A tank or container of fluid is simply suspended at a height of h above the sweat simulator device. This allows fine and repeatable adjustment of flow rate by adjusting h (therefore adjusting hydrostatic pressure) and more importantly sustains a very low pressure required for low flow rate through the sweat simulator device. Now that the fundamental features of the sweat simulator system are described, a theoretical model can be developed.

The theoretical model is presented for the bi-layer design, a design which produces uniform flow rate at all sweat pores (Fig. 1b, Fig. 2b). A fluid resistance network approach (Fig. 2c) was used to calculate the fluid flow rate (Q, L h^{-1}), and therefore the simulated 'sweat' rate densities (V, L h^{-1} m^{-2}). First, equilibrium conditions are assumed where the driving pressure (P_0) will be dropped across the top sweat pore layer (P_S) and the bottom membrane layer (P_m):

$$P_0 = P_m + P_S \tag{1}$$

Note that the pressure drop in the hydrophilic tubing connecting the tank and the 'sweat' simulator chamber is ignored because it has much smaller fluid resistance (id = 1 mm tube). The bottom membrane is hydrophilic enough such that Laplace pressure does not contribute to P_m (fluid readily wets through it and onto its exposed surface). Pressure drop in the bottom membrane (P_m) is therefore only due to the fluid resistance of the membrane (R_m), as given by

$$P_m = R_m \times Q_n \tag{2}$$

where Q_n is the fluid flow rate (L h^{-1}).

At this point, the theoretical development will focus on a single 'sweat' pore in the top layer. For one 'sweat' pore in the top layer with a diameter D_S, the fluid resistance in the bottom membrane can be calculated as:

$$R_m = \frac{128\mu L_m}{\pi D_m^4} \times \frac{1}{\pi D_S^2 \alpha/4} \tag{3}$$

where L_m is the membrane thickness, D_m is the membrane pore diameter, μ is the viscosity of the fluid, and α is the membrane pore density ($\pi D_S^2\alpha/4$ is the amount of pores in the membrane under one 'sweat' pore in the top layer).

Next, pressure drop in the top 'sweat' pore (P_S) can be calculated from:

$$P_S = R_S \times Q_n + P_L \tag{4}$$

where R_S is the fluid resistance in one 'sweat' pore and P_L is the Laplace pressure, and are calculated respectively as,

$$R_S = \frac{128\mu L_S}{\pi D_S^4} \tag{5}$$

$$P_L = \frac{4\gamma\cos(\theta_a)}{D_S} \tag{6}$$

where L_S is the membrane thickness of the 'sweat' pore layer, γ is the surface tension of the fluid, and θ_a is the advancing contact angle for the fluid in the sweat pore. As a reminder, once fluid wets out onto the outer surface of the top sweat pore layer, Laplace pressure becomes small enough that it can be ignored.

The bottom membrane is selected such that the fluid resistance in the bottom membrane is much larger than the resistance in the top sweat pore layer ($R_m \gg R_S$), which requires the bottom membrane pore diameter to be $D_m << \sqrt[4]{4D_S^2 L_m/(\pi\alpha L_S)}$. The fluid flow rate ($Q$, L h^{-1}) in one 'sweat' pore for the bi-layer design can then be calculated as follows:

$$Q_n = \frac{\pi^2 D_m^4 D_S \alpha[\rho g h D_S - 4\gamma\cos(\theta)]}{512\mu L_m} \tag{7}$$

The fluid flow rate density or 'sweat' rate density (V_n, L h^{-1} m^{-2}) in one 'sweat' pore area of πD_S^2 is then calculated as:

$$V_n = \frac{\pi D_m^4 \alpha[\rho g h - 4\gamma\cos(\theta)/D_S]}{512\mu L_m} \tag{8}$$

For the fabricated artificial microfluidic skin with a 'sweat' pore density of ω, the 'sweat' rate density (L h^{-1} m^{-2}) for the artificial microfluidic skin is therefore:

$$V = \frac{\omega\pi^2 D_m^4 D_S \alpha[\rho g h D_S - 4\gamma\cos(\theta)]}{512\mu L_m} \tag{9}$$

This model does not include effects of evaporation *vs.* droplet size,[25] as our rough calculations determined evaporation to be inconsequential with respect to the flow rates and Laplace pressures driving the model. With a theoretical model for 'sweat' rate density now in-hand, and dimensional constraints better understood, we can now discuss the fabrication of the artificial microfluidic skin.

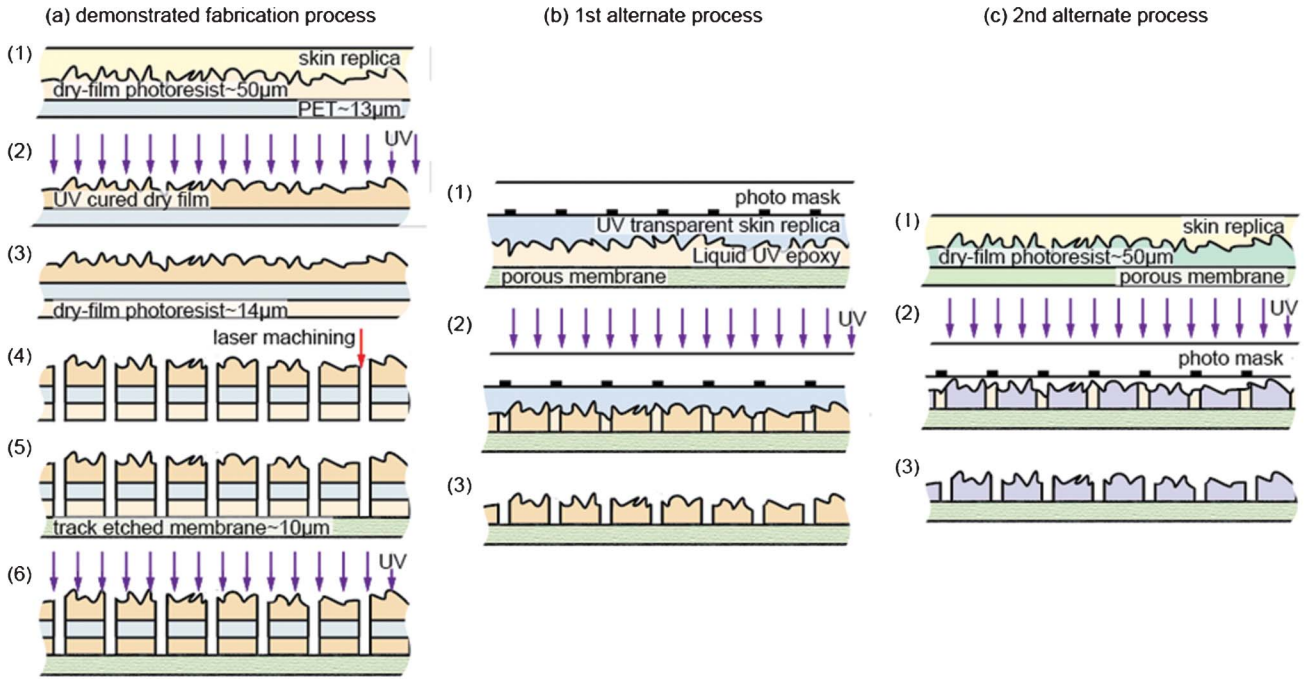

Fig. 3 Descriptive artwork of three optional fabrication processes for fabricating bi-layer artificial 'skin' membranes. Prototypes demonstrated are fabricated with process (a), and alternates shown in (b) and (c) are proposed and have not yet been explored or demonstrated. Aspect ratios for the sweat pores and photoresist/membrane thickness are not representative in the diagram.

Fabrication

The bi-layer artificial microfluidic skin features a top layer with 'skin' textures and 'sweat pores', and a bottom membrane which regulates flow rate. Fabrication for each of them can be achieved easily with standard microfabrication techniques, such as micro-replication and photolithography. Surprisingly, it was discovered that the most challenging issue was how to bond the two layers without damaging the functionality of the bottom membrane layer.

The initial process we have demonstrated is fairly simple, requires no photolithography or alignment, and results in flexible artificial skins with all the requisite features needed for perspiration simulation. The fabrication starts with applying Silflo™ replica resin (CuDerm Corp.) to human skin and peeling to make an inverse mold of skin texture (the lead author's forearm was utilized). This silicone mold is then used to hot emboss skin texture (Fig. 3a-1) into 50 μm thick membrane of DuPont PerMX dry film photoresist layer carried on an underlying ~13 μm polyester film (vacuum plate hot embossing, 10 PSI vacuum applied then heated to 55 °C). The embossed photoresist is then UV cured (Fig. 3a-2). Next an additional 14 μm PerMX dry layer is laminated underneath the polyester (Fig. 3a-3), and will later serve as an adhesive layer. 'Sweat' pores of ~80 μm diameter are then laser micro machined (Fig. 3a-4) using an Universal Laser Systems VLS3.60 system. Higher resolution holes are certainly possible with more advanced laser milling systems or the fabrication techniques of Fig. 3b, 3c, but were not necessary to complete this work. Lastly, a ~10 μm thick track etched polycarbonate membrane (hydrophilic, D_m ~ 0.2 μm pores, pore density of ~3 × 10^8 per cm^2, Sterlitech) is hot-roll laminated (70 °C, 40 PSI, Western Magnum XRL-120) to the bottom adhesive PerMX layer (Fig. 3a-5) and UV cured to crosslink the adhesive photoresist (Fig. 3a-6). Since the thickness of the bottom adhesive PerMX layer is much smaller compared to the diameter of the laser milled sweat pores, the pores will not become blocked during hot-roll laminating. An SEM photo of the fabricated artificial microfluidic skin membrane is shown in Fig. 4b. The final membrane was ~2″ diameter with measurable groove depth and texture ranging from <1 μm to maximum of ~50 μm amplitude, and with an average of D_s ~ 80 μm diameter pores at a density of ω ~ 2 pores/mm^2.

For sweat simulators that require smaller and higher resolution pores, two optional photolithography processes are also proposed and listed in Fig. 3b, 3c. For process (b), 'skin' texture and 'sweat' pores are photolithographically patterned at one time with UV epoxy sandwiched between a UV transparent skin replica mold/photomask and porous membrane. This simplified process can fabricate much smaller and higher resolution 'sweat' pores with photolithography, but will require the membrane to be chemically and physically resistant to the chemicals and temperatures used. For process (c), skin texture is hot-embossed into a dry film photoresist or a soft-baked (dry) layer of liquid photoresist on top of the porous membrane, and then the sweat pores are patterned by photolithography. Again, chemical/temperature compatibility will be needed. The polycarbonate track etched

membranes used in this work are not compatible with such fabrication in terms of temperature or chemical stability. Perhaps polyimide track etched membranes would suffice, if they could be rendered highly hydrophilic while the top skin-texture membrane remained more neutrally hydrophilic/hydrophobic.

Once the artificial microfluidic skin membranes are fabricated, they are integrated into a mechanically milled acrylic holder to create the sweat simulator (Fig. 1c). The artificial microfluidic skin membrane is sealed with epoxy on top of the acrylic container, or o-ring clamped, and the formulated sweat is fed into the acrylic chamber through tubing from the tank suspended above the setup by an adjustable *z*-axis track (Codan BC574, id $\sim$ 1 mm).

Results and discussion

The wetting characteristics of the artificial microfluidic skin were first explored with saline solution (0.3 w.t.%),[17] and it was found that the artificial skin could replicate the wetting of human skin with reasonable satisfaction for this initial work. As shown in Fig. 4, the contact angle of the artificial skin was measured at $\sim$76° advancing and $\sim$38° receding, which was less hydrophobic than the authors human skin measured at $\sim$118° advancing and $\sim$78° receding contact angles. 10 μl saline droplets were also placed on both human and artificial skin, the surfaces tilted vertically, to also confirm the presence of wetting hysteresis (Fig. 4). The sweat simulator device shown in Fig. 1c was then tested with the 'sweat' tank level at h = 28 mm (0.4 psi). Artificial sweat generation can be seen for multiple 'sweat' pores in Fig. 5a and a single 'sweat' pore in Fig. 5b. Using a Slimline Glass flowmeter (Gilmont), the averaged flow rate for a single pore was calculated to be $\sim 8.2 \times 10^{-7}$ L h^{-1}, which is comparable to the average sweat rate of 5.8×10^{-7} L h^{-1} per sweat pore for runners.[17] Importantly, the skin texture has strong influence on the shape and wetting path of the sweat. The last frame of the photos in Fig. 5b clearly shows the effect of pinning[26] and diverging/converging wetting surfaces.

These experimental results confirm that artificial skin can provide wetting hysteresis and pinning effects expected for a textured surface. However, further wetting exploration or optimization was not explored for several reasons. Firstly, it is not possible with reasonable effort to understand the exact wetting characteristics of human skin and make comparison to our artificial results, as little of such information is available. Furthermore, different human subjects will have different levels of skin oil, roughness, dryness, *etc*. Therefore although these first results appear promising, and are likely satisfactory for rudimentary application, some applications may require optimization for a wide range of scenarios (*e.g.* skin wetting of hydrated *vs.* dry skin, or clean skin *vs.* after application of sunscreen). If such optimization is required, simple surface energy treatments can be implemented to increase or decrease the hydrophobicity of the artificial skin.

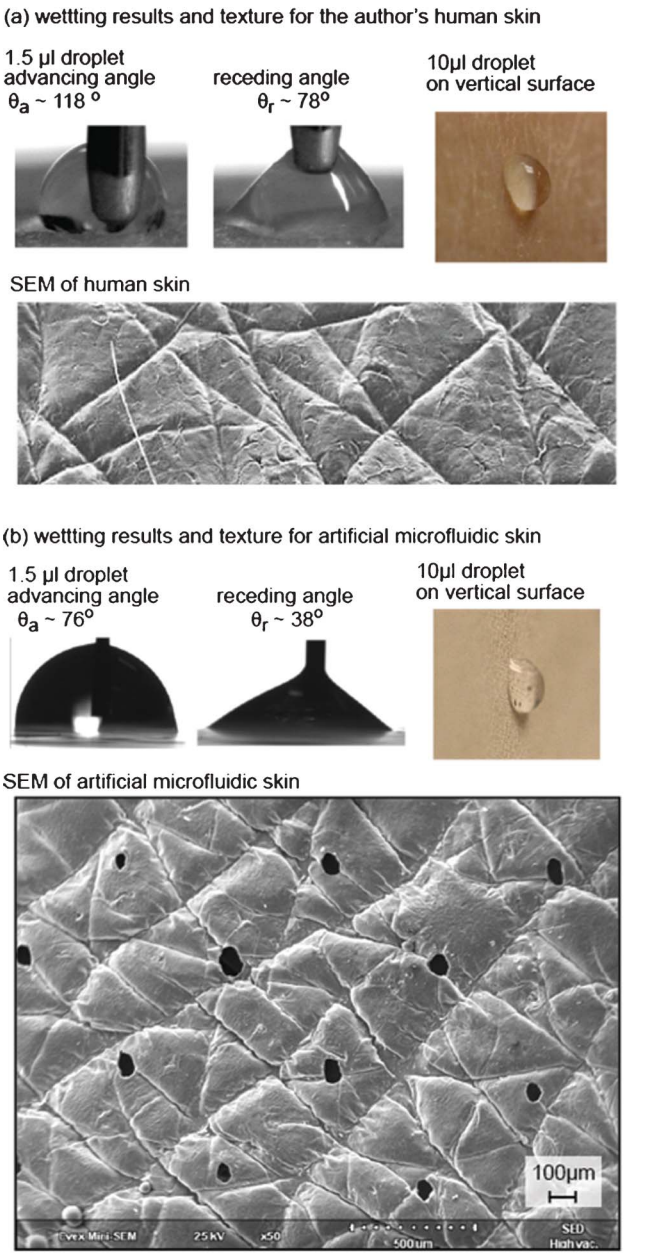

Fig. 4 (a) SEM photography of human skin[24] and related droplet contact angles, and (b) SEM photography of the fabricated artificial microfluidic skin and related droplet contact angles. Although variation in sweat pore size is obvious in the SEM photograph of (b), the artificial skin was designed to minimize/eliminate the associated influence of variation in Laplace pressure with pore size.

The next characterization performed was to confirm that the 'sweating' velocity can be uniform and adjustable with pressure, and to perform as predicted by the theoretical model. The liquid tank height h was adjusted from 25 cm (0.36 psi) to 45 cm (0.85 psi) and experimentally measured sweat velocities are plotted in Fig. 6. It should be noted that the minimum initial pressure required to start flow through the membrane was $\sim$0.4 psi for $\sim$1 s, and once flow was started,

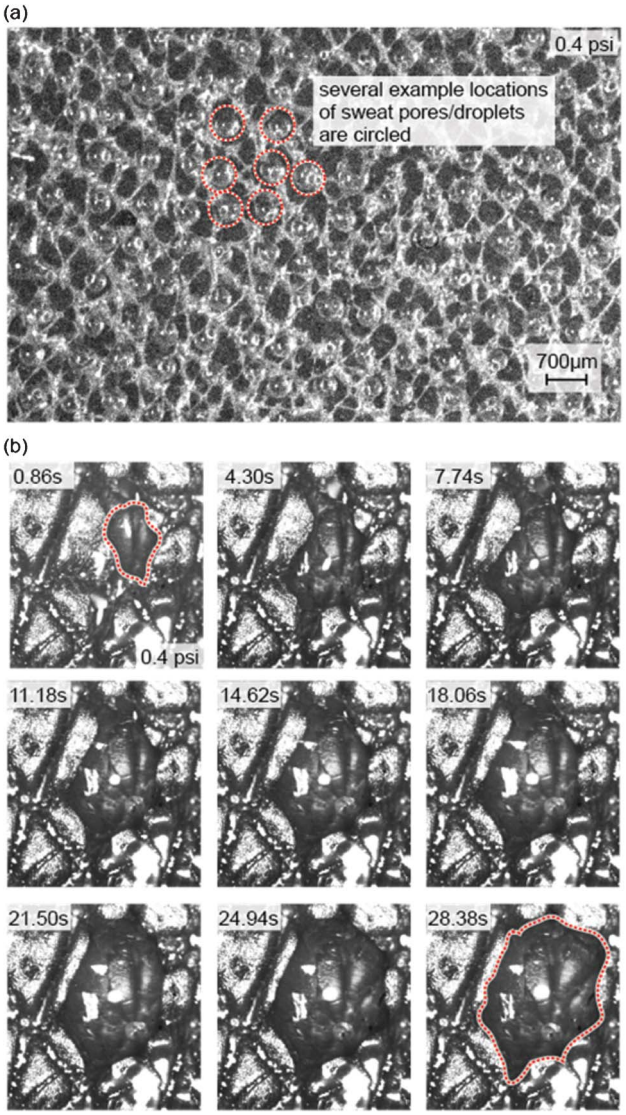

Fig. 5 Photos of 'sweating' (a) multiple artificial sweat pores and (b) over a single sweat pore, for an applied pressure of 0.4 psi. Although nearly all pores are activated, it is difficult to visualize all of them as the artificial skin has rough surface which also scatters reflected light. Therefore in Fig. 5a, a few red circles are added to identify a subset of activated pores, and similar red outline is also provided in Fig. 5b to help visualize the wetting perimeter (contact line) of the droplet emerging from a pore.

pressure could be further increased or decreased to modify flow rate. The experimental data were recorded with the Slimline Glass flowmeter (Gilmont) for each data point after the flow rate was stabilized. The data were taken after fluid wets on the exposed surface of the top sweat pore layer, and therefore Laplace pressure effects become insignificant (see inset diagram for Fig. 6). If Laplace pressure can be ignored, then eqn (7) and (9) can then be simplified to:

$$Q_{\mathrm{n}}^{'} = \frac{\rho g h \pi^2 D_{\mathrm{m}}^4 D_{\mathrm{S}}^2 \alpha}{512 \mu L_{\mathrm{m}}} \tag{10}$$

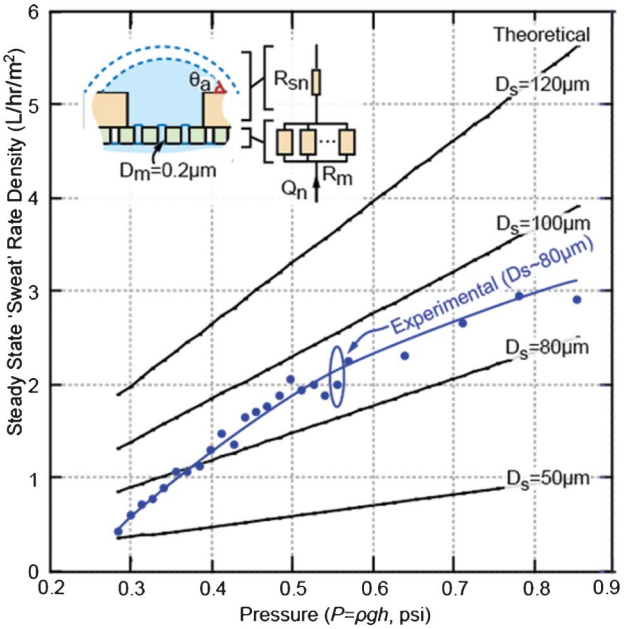

Fig. 6 Theoretical and experimental results for steady state 'sweat' rate density *vs.* pressure for the fabricated artificial microfluidic skin. The average experimental pore size was 80 μm. The inset diagram represents the wetting condition and microfluidic model during which the data was calculated or measured.

$$V^{'} = \frac{\omega \rho g h \pi^2 D_{\mathrm{m}}^4 D_{\mathrm{S}}^2 \alpha}{512 \mu L_{\mathrm{m}}} \tag{11}$$

Eqn (10) and (11) are then used to generate the theoretical data presented in Fig. 6. The experimental results shown are with a pore diameter average of $D_s \sim 80$ μm, and are in general agreement with the theoretically expected results. These results also confirm that the artificial microfluidic skin can simulate sweat levels associated with human exercise (0.75 L h^{-1} m^{-2} for runners[17]). There are three additional observations regarding the experimental results of Fig. 6, which are worthy of discussion. First, initially the increase in perspiration rate with increasing pressure is non-linear and greater than that theoretically predicted. This effect is at least partially due to initial expansion of flexible artificial skin membrane[27] (*e.g.* as seen in Fig. 1c, the membrane could be seen to expand as pressure is initially ramped, which creates additional volume below the membrane that must be filled, which then temporarily increases the measured flow rate feeding into the device). Second, higher theoretical perspiration rates, beyond human rates, are also provided in Fig. 6 because for some applications this might shorten the required testing time, or provide new experimental insights. Third, the perspiration variation between individual pores was not measured for the artificial microfluidic skin, because little is known about human sweat gland variance (practically it might not be that important). As observed in Fig. 5a, all pores are

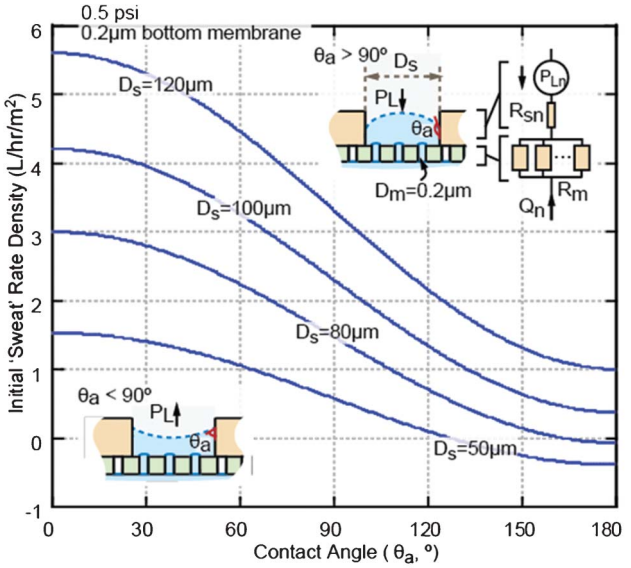

Fig. 7 Theoretical plots of initial 'sweat' rate density *vs.* contact angle at 0.5 psi. The inset diagram represents the wetting condition and microfluidic model during which the data was calculated.

activated and contributing to the perspiration rate in a fairly even manner.

To further reduce the sweat flow rate densities to match human sweating in more sedentary activities, membranes can be made with either or both of two modifications: increased pressure drop in the bottom flow-limiting membrane; smaller 'sweat' pore diameter D_s in the top layer. Several different hydrophilic track etched polycarbonate membranes (Sterlitech) were then tested for decreasing the sweat flow rate densities, including track etched pores of 0.1 μm and 0.03 μm, of various pore densities. Testing failed to generate a uniform flow rate among sweat pores with liquid pressures applied up to 0.85 psi, possibly due to a higher liquid pressure required for uniform activation of all pores, which can be resolved if a super hydrophilic track etched membrane is obtained. Therefore, at this time 0.2 μm pores are preferred based on experimental results. To further reduce the flow rate densities, smaller pore diameter is therefore necessary in the top layer. However, smaller pores will give rise to greater effects of Laplace pressure as fluid first starts to flow into these pores (called initial 'sweat' velocity). To explore what can theoretically be done, the initial 'sweat' velocity (eqn (9)) is plotted *vs.* advancing contact angle with 0.5 psi driving pressure (Fig. 7, again same 0.2 μm pore track etched membrane with L_m of 10 μm). The most important conclusion from this analysis is as follows. Pore diameters can be reduced down to ~50 μm, possibly even further, if the pores are adequately hydrophilic, reducing the flow rate density by ~60% (reduced area ratio $(50/80)^2$). If the pores are hydrophobic, some cases for the advancing contact angle show a zero or negative sweat velocity, which is when the applied pressure for creating flow is inadequate to overcome Laplace pressure in the sweat pore. The plots of Fig. 7 also show that expected flow rate densities of Fig. 6 are not valid until 'sweat' wets out onto the outer skin surface.

Conclusions

An artificial microfluidic skin has been created for simulating human skin perspiration. The fabrication process used was simple, using mainly simple lamination and laser milling techniques. The results provide uniform sweat rate among fabricated sweat pores, and sweat rate densities comparable with human exercise, with lower sweat rate densities likely achievable by reducing the size of sweat pores. A theoretical model was developed, which predicts sweat rate densities based on microfluidic geometries and contact angles, and the model was found to be in general agreement with the experimental results. The demonstrated artificial microfluidic skin should prove to be a viable *in vitro* perspiration substitute for some human or animal subject testing. Future work will focus on reducing the 'sweat' pore radius and therefore minimum perspiration rates, and will focus on reducing the surface energy to that more similar to skin.

Acknowledgements

This work was supported by the Air Force Research Laboratory, BSEM program in the Materials and Manufacturing Directorate. The authors would also like to thank Doug Hurd, and Jeffrey Simkins for their help on machining the acrylic chambers.

References

1 K. Wilke, A. Martin, L. Terstegen and S. S. Biel, *Int. J. Cosmet. Sci.*, 2007, **29**, 169–179.
2 E. M. Jackson, *Skin Pharmacol. Physiol.*, 1999, **12**, 125–131.
3 Z. D. Draelos and R. Norman, *Preventive Dermatology*, 2010, **2**, 173–186.
4 Z. D. Draelos, *Dermatol. Ther.*, 2012, **25**, 223–228.
5 C. J. Smith and G. Havenith, *The Fourth International Conference on Human-Environment System (ICHES 2011)*, 2011, 782–787.
6 L. Jun, R. L. Barker and A. S. Deaton, *Text. Res. J.*, 2007, **77**, 59–66.
7 H. J. Liberty, B. D. Johnson and N. Fortner, *J. Anal. Toxicol.*, 2004, **28**, 667–673.
8 E. J. Cone, M. J. Hillsgrove, A. J. Jenkins, R. M. Keenan and W. D. Darwin, *J. Anal. Toxicol.*, 1994, **18**, 298–305.
9 D. A. Kidwell, J. C. Holland and S. Athanaselis, *J. Chromatogr., Biomed. Appl.*, 1998, **713**, 111–135.
10 P. Kintz, A. Tracqui, P. Mangin and Y. Edel, *J. Anal. Toxicol.*, 1996, **20**, 393–397.
11 G. Cizza, A. H. Marques, F. Eskandari, I. C. Christie, S. Torvik, M. N. Silverman, T. M. Phillips and E. M. Sternberg, *Biol. Psychiatry*, 2008, **64**, 907–911.
12 A. H. Marques, M. N. Silverman and E. M. Sternberg, *NeuroImmunoModulation*, 2010, **17**, 205–208.

13 S. Coyle, K. Lau, N. Moyna, D. O'Gorman, D. Diamond, F. Di Francesco, D. Costanzo, P. Salvo, M. Trivella, D. De Rossi, N. Taccini, R. Paradiso, J. Porchet, A. Ridolfi, J. Luprano, C. Chuzel, T. Lanier, F. Revol-Cavalier, S. Schoumacker, V. Mourier, I. Chartier, R. Convert, H. De-Moncuit and C. Bini, *IEEE Trans. Inf. Technol. Biomed.*, 2010, **14**, 364–370.
14 D. H. Kim, N. Lu, R. Ma, Y. S. Kim, R. H. Kim, S. Wang, J. Wu, S. M. Won, H. Tao, A. Islam, K. J. Yu, T. I. Kim, R. Chowdhury, M. Ying, L. Xu, M. Li, H. J. Chung, H. Keum, M. McCormick, P. Liu, Y. W. Zhang, F. G. Omenetto, Y. Huang, T. Coleman and J. A. Rogers, *Science*, 2011, **33**, 838–843.
15 R. Paradiso and D. De Rossi, *Conf. Proc. IEEE Eng. Med. Biol. Soc.*, 2006, **1**, 392–395.
16 S. Roy, G. De Luca, M. Cheng, A. Johansson, L. Gilmore and C. De Luca, *Med. Biol. Eng. Comput.*, 2007, **45**, 447–457.
17 S. D. Henkin, P. L. Sehl and F. Meyer, *Int. J. Sports Physiol. Perform.*, 2010, **5**, 359–366.
18 J. Venkataraman and B. Freer, *IEEE Int. Symp. Antennas Propag. 2011*, 2011, 603–606.
19 http://www.2spi.com/catalog/spec_prep/filter6.shtml.
20 http://www.sterlitech.com/membrane-disc-filters/polycarbonate-membranes.html.
21 J. Hagen, S. Kim, B. Bayraktaroglu, K. Leedy, J. Chavez, N. Kelley-Loughnane, R. Naik and M. Stone, *Sensors*, 2011, **11**, 6645–6655.
22 J. Hagen, S. Kim, N. Kelley-Loughnane, R. Naik and M. Stone, Chemical, Biological, Radiological, Nuclear, and Explosives (CBRNE) Sensing Xii, *Proc. SPIE–Int. Soc. Opt. Eng.*, 2011, **8018**, 80180B-1–6.
23 D. Rose, *Printed and Flexible Electronics Technology for Health, Safety and Biosensor Applications Workshop*, 2013.
24 Y. W. Linde, A. Bengtsson and M. Loden, *Acta Derm Venereol*, 1989, **69**, 315–319.
25 H. Song, Y. Lee, S. Jin, H. Kim and J. Yoo, *Microelectron. Eng.*, 2011, **88**, 3249–3255.
26 Y. Kalinin, V. Berejnov and R. Thorne, *Langmuir*, 2009, **25**, 5391–5397.
27 The membrane flexing had no implication on adhesion between any layers of the device, and was so small that there was no measurable effects on flow rate. Theoretical calculations predict that the maximum increase in flow rate is only $\sim$0.5% at maximum flexing.